



RESEARCH ARTICLE

Predicting catchment-scale methane fluxes with multi-source remote sensing

Aleksi Räsänen · Terhikki Manninen · Mika Korkiakoski · Annalea Lohila · Tarmo Virtanen

Received: 25 August 2020 / Accepted: 18 January 2021 / Published online: 10 February 2021
© The Author(s) 2021

Abstract

Context Spatial patterns of CH₄ fluxes can be modeled with remotely sensed data representing land cover, soil moisture and topography. Spatially extensive CH₄ flux measurements conducted with portable analyzers have not been previously upscaled with remote sensing.

Objectives How well can the CH₄ fluxes be predicted with plot-based vegetation measures and remote sensing? How does the predictive skill of the model change when using different combinations of predictor variables?

Supplementary Information The online version contains supplementary material available at <https://doi.org/10.1007/s10980-021-01194-x>.

A. Räsänen (✉) · T. Virtanen
Ecosystems and Environment Research Programme,
Faculty of Biological and Environmental Sciences, and
Helsinki Institute of Sustainability Science (HELSUS),
P.O. Box 65, 00014 University of Helsinki,
Helsinki, Finland
e-mail: aleksi.rasanen@helsinki.fi

T. Manninen · M. Korkiakoski · A. Lohila
Finnish Meteorological Institute, P.O. Box 503,
000101 Helsinki, Finland

A. Lohila
INAR Institute for Atmospheric and Earth System
Research/Physics, Faculty of Science, P.O. Box 68,
00014 University of Helsinki, Helsinki, Finland

Methods We measured CH₄ fluxes in 279 plots in a 12.4 km² peatland-forest-mosaic landscape in Pallas area, northern Finland in July 2019. We compared 20 different CH₄ flux maps produced with vegetation field data and remote sensing data including Sentinel-1, Sentinel-2 and digital terrain model (DTM).

Results The landscape acted as a net source of CH₄ (253–502 µg m⁻² h⁻¹) and the proportion of source areas varied considerably between maps (12–50%). The amount of explained variance was high in CH₄ regressions (59–76%, nRMSE 8–10%). Regressions including remote sensing predictors had better performance than regressions with plot-based vegetation predictors. The most important remote sensing predictors included VH-polarized Sentinel-1 features together with topographic wetness index and other DTM features. Spatial patterns were most accurately predicted when the landscape was divided into sinks and sources with remote sensing-based classifications, and the fluxes were modeled for sinks and sources separately.

Conclusions CH₄ fluxes can be predicted accurately with multi-source remote sensing in northern boreal peatland landscapes. High spatial resolution remote sensing-based maps constrain uncertainties related to CH₄ fluxes and their spatial patterns.

Keywords Methane flux measurements · Geographic object-based image analysis · Lidar · Satellite imagery · Synthetic aperture radar · Vegetation mapping

Introduction

Methane (CH_4) is the second most important greenhouse gas (IPCC 2013), and a large part of CH_4 emissions originate from northern peatlands (Frolking et al. 2011; Turetsky et al. 2014; Abdalla et al. 2016). On the one hand, CH_4 is produced by methanogens in anoxic conditions, which are typically obtained in water-saturated conditions in which diffusion of gases is low and oxygen is depleted quickly. CH_4 is transported from soil to the atmosphere by molecular diffusion, in the form of gas bubbles (i.e. ebullition) and plant-mediated processes. On the other hand, CH_4 can be oxidized to carbon dioxide by CH_4 consuming methanotrophs in oxic conditions, typically found in the surface peat layers. A net emission into the atmosphere is observed when production and transport exceed consumption (Le Mer and Roger 2001; Lai 2009; Abdalla et al. 2016).

Important factors controlling CH_4 emissions are soil temperature, water table depth, plant community composition, and soil pH (Turetsky et al. 2014; Abdalla et al. 2016). These factors are spatially heterogeneous in diverse scales in the landscape, and there are considerable uncertainties in the resulting net emission of CH_4 by the peatlands and how the emissions are distributed spatially (Turetsky et al. 2014). In some circumstances, also mineral soils can act as CH_4 sources (Lohila et al. 2016). To constrain the different uncertainties, there have been attempts to assess and upscale CH_4 flux patterns over different spatial extents ranging from a single mire (Lehmann et al. 2016) to landscapes (Dinsmore et al. 2017) and also to synthesize CH_4 controls globally (Turetsky et al. 2014).

The spatial patterns of CH_4 fluxes can be assessed with remote sensing-based maps. One approach is to monitor CH_4 fluxes with imaging spectroscopy, in particular in shortwave and thermal infrared region. However, this approach has been limited to CH_4 plumes instead of diffuse fluxes originating from peatlands (Thorpe et al. 2016). Coarse-grained estimates of CH_4 fluxes can be derived with large scale process models resembling carbon cycle (Bruhwiler et al. 2014) or more locally with the eddy covariance method (Davidson et al. 2017). However, in spatially heterogeneous landscapes, such as forest-peatland mosaics, CH_4 fluxes have fine-scale spatial heterogeneity. Therefore, a typical approach is to measure

fluxes with chambers and then upscale of the observations with remote sensing data (Lehmann et al. 2016; Dinsmore et al. 2017; Morozumi et al. 2019).

Chambers can measure fluxes only from a small area ($< 0.5 \text{ m}^2$), and the number of chamber plots is limited in one study; therefore, there remain large uncertainties whether the limited number of chamber plots are representatively sampled over a specific landscape (Lehmann et al. 2016; Davidson et al. 2017). A typical approach is to upscale fluxes with categorical land cover maps (Lehmann et al. 2016; Morozumi et al. 2019), and it has been shown that more accurate upscaling can be derived with land cover maps with higher thematic resolution (Lehmann et al. 2016). However, it has been discussed that maps of continuous variables (e.g. topographic features, spectral indices and tree canopy cover) represent more accurately landscape processes such as CH_4 fluxes, which are typically not limited to crisp patches (McGarigal et al. 2009; Kedron et al. 2018). Therefore, another option is to conduct CH_4 upscaling with continuous maps of specific property such as satellite-derived spectra (Dinsmore et al. 2017).

It is possible to link CH_4 fluxes to diverse remotely sensed or other data sources. In numerous mapping endeavors it has been shown that multi-source remote sensing (i.e. inclusion of multiple types of remotely sensed information in one mapping workflow) increases the accuracy (Bourgeau-Chavez et al. 2016; Karlson et al. 2019; Räsänen and Virtanen 2019). As CH_4 fluxes in northern landscapes are mainly connected to peatlands, it can be assumed that similar methods can be used for detection of peatlands and tracking spatial patterns of CH_4 . In previous studies, it has been shown that multiple remote sensing datasets are useful in wetland and peatland delineation, containing optical data depicting spectral properties of vegetation and land cover (Bourgeau-Chavez et al. 2016; Minasny et al. 2019), synthetic aperture radar (SAR) data sensitive to moisture, surface roughness and vegetation structure (Widhalm et al. 2015; Bourgeau-Chavez et al. 2016; Millard and Richardson 2018; Karlson et al. 2019; Minasny et al. 2019) and topographic data capable to model presumably wet areas based on water flow routes and flatness (Murphy et al. 2007; Karlson et al. 2019; Minasny et al. 2019; Lidberg et al. 2020). Nonetheless, the use of multi-source remote sensing data has been limited in CH_4 flux studies. Furthermore, recent technological

development of portable CH₄ measurement devices has opened up possibilities for spatially dense and extensive field sampling. However, to the best of our knowledge, spatially extensive measurements have not yet been linked to remotely sensed data.

We measured CH₄ fluxes with spatially extensive chamber measurements ($n = 279$) in two adjacent catchments (altogether 12.4 km²) in northern Finland covering all main land cover types in the area during a two-week period in early July 2019. We then upscaled the measurements to the whole study area with multi-source remote sensing data including Sentinel-2 optical satellite imagery, Sentinel-1 SAR data and topographic data. Our two research questions were: How well can the CH₄ fluxes be predicted with plot-based vegetation measures and remote sensing data representing land cover, soil moisture and topography? How does the predictive skill of the model change when using different combinations of predictor variables?

Materials and methods

Study area

We studied landscape-level CH₄ fluxes in two adjacent catchments (4.5 km² and 7.9 km² respectively) in Pallas area, located in Muonio municipality, in northern Finland (67°57'–68°01' N; 24° 10'–24°15' E, Fig. 1). The area belongs to northern boreal vegetation zone and subarctic climate zone with the annual average temperature being −1.3 °C, precipitation 547 mm, and the number of growing degree days above 5 °C 698 (years 1981–2010, data from nearby Kittilä Pokka station). The area is characterized by gently undulating terrain with the elevation above sea level ranging between 267 and 564 m. According to our land cover classification, coniferous and mixed coniferous-deciduous forests (68%) and forested and open peatlands (17%) dominate the whole area, while its western part includes mountain tundra and treeline vegetation (14%) (Fig. 1, Table 1; methods described in Supplementary material). Dominating tree species include Norway spruce (*Picea abies*), Scots pine (*Pinus sylvestris*) and Downy birch (*Betula pubescens*). The western part of the study area belongs to Pallas-Yllästunturi National Park and includes old-growth forests, mostly with mixed tree

species composition (Fig. 1). The eastern part contains mostly coniferous dominated forests, as in the latter half of the twentieth century, deciduous trees were selectively logged, and Scots pines were planted in some locations. Furthermore, some of the peatlands in the eastern part have been drained for forestry purposes in the same period. Atmospheric, ecological and hydrological research within and nearby the study area has been extensive during the past decades (Lohila et al. 2015).

Field inventory and vegetation data

We gathered the vegetation cover data and conducted the CH₄ flux measurements between July 3 and 13, 2019 in twelve 0.5–2.0 km long transects located within the catchments so that all major land cover types were included (Fig. 1). Along each transect, we sampled circular plots with 10 m diameter in 100 m intervals. Within most of the circular plots, we sampled three subplots with 0.5 m diameter located at a 2 m distance to the north, east, and west from the plot centroid. In total, we sampled 131 larger plots and 300 subplots. We collected the location of each plot with Trimble R8 GPS device with ± 0.05 m accuracy.

For each plot, we calculated a number of plot-based vegetation measures representing vegetation composition and structure. In the larger plots, we measured the height, crown length and diameter at breast height of each tree located within the plot. Within the subplots, we estimated %-cover of each vascular plant and moss species and measured the average height of each vascular plant species. For each larger plot, we estimated the ground and field layer biomass and leaf-area index for four vascular plant functional types (evergreen shrubs, deciduous shrubs, forbs, and graminoids) and biomass for mosses as well as total biomass and leaf-area index (Supplementary material). Additionally, we estimated tree biomass and leaf-area index for spruce, pine, coniferous trees in total, deciduous trees in total, and all trees in total (Supplementary material). For each subplot, we defined membership values for fuzzy plant community clusters (Supplementary material).

At each of the 279 subplots, we conducted chamber-based measurements of CH₄ fluxes once during the field inventory period. The chamber closure time was always 5 min and measurements took place

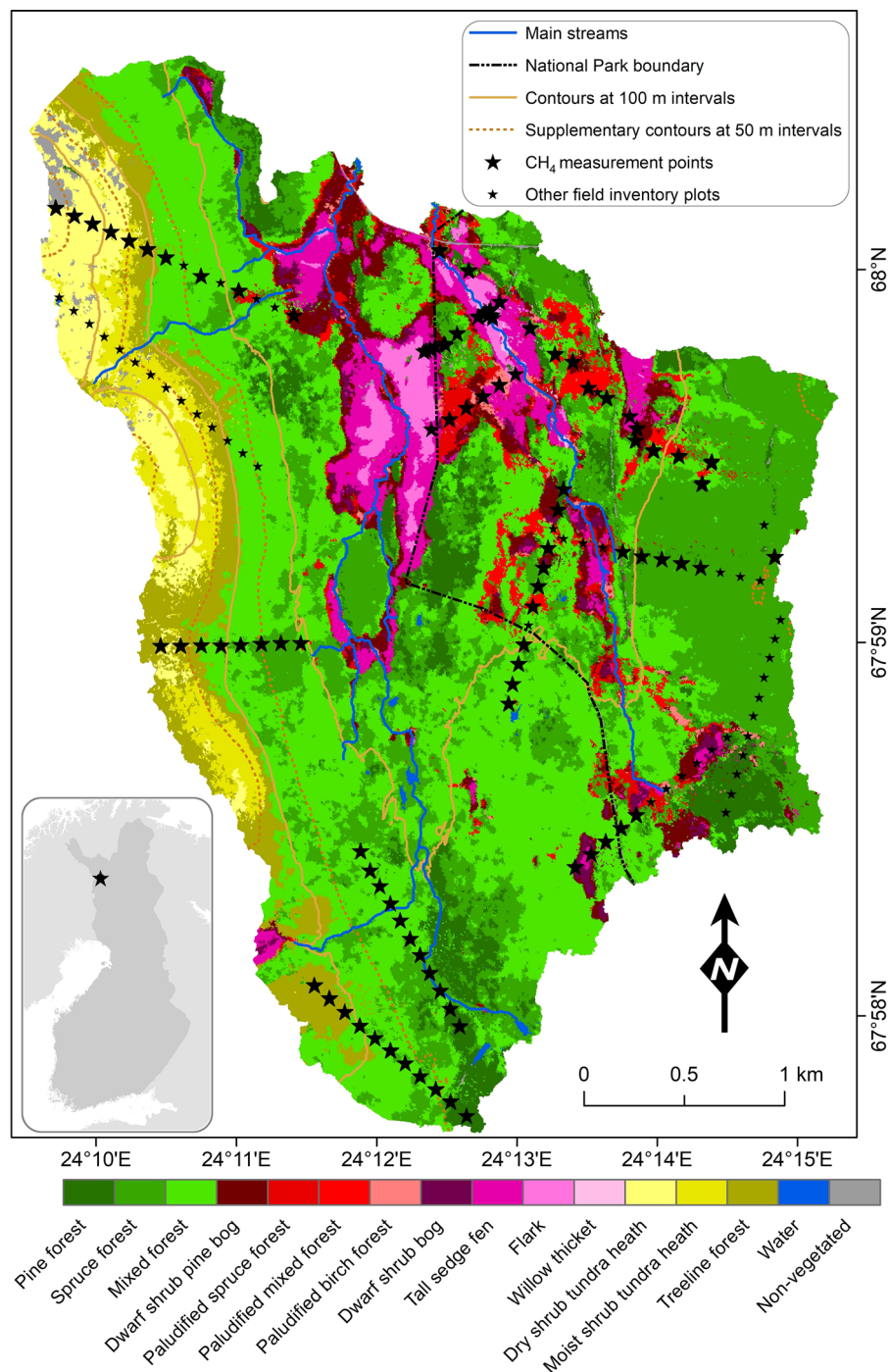


Fig. 1 Land cover map of the study area located in northern Finland. The classification accuracy was 76% and methods description is given in Supplementary material

between 9:15 AM and 5:30 PM. We used portable LI-COR trace gas analyzer (LI-7810, LI-COR Environmental, Lincoln, NE, USA) and a closed opaque

chamber (height 30.5 cm, diameter 31.5 cm). During the flux measurements, we measured the air temperature inside the chamber headspace. We measured soil

Table 1 Description of different land cover types, their %-cover in the landscape and number of methane measurement plots

Land cover type	Description	%-cover	CH ₄ plots
Forests on mineral soil		68.0	144
Pine forest	Pine-dominated forest on mineral soil; canopy cover at least 20%; pine (<i>Pinus sylvestris</i>) cover at least 2/3 of total canopy cover; field layer dominated by evergreen shrubs (esp. <i>Vaccinium vitis-idaea</i>); some deciduous shrubs may exist; ground layer dominated by feather mosses and lichens	7.1	24
Spruce forest	Spruce-dominated forest on mineral soil; canopy cover at least 20%; Norway spruce (<i>Picea abies</i>) cover at least 2/3 of total canopy cover; field layer dominated by deciduous shrubs (esp. <i>Vaccinium myrtillus</i>), also evergreen shrubs, forbs and graminoids exist; ground layer dominated by feather mosses	26.4	54
Mixed forest	Forest on mineral soil; canopy cover at least 20%; not dominated by one species, dominant tree species include pine, spruce and birch (<i>Betula pubescens</i>), the cover of minority species at least 1/3; field layer dominated by deciduous shrubs, forbs and graminoids; ground layer dominated by mosses and lichens	34.5	66
Peatlands		17.2	102
Dwarf shrub pine bog	Peatland with coverage of pines at least 1%; evergreen (<i>Rhododendron tomentosum</i>) and deciduous (<i>Vaccinium uliginosum</i> , <i>Betula nana</i>) shrubs dominate in field layer, also some forbs (<i>Rubus chamaemorus</i>) and graminoids (mostly <i>Carex</i> spp.); ground layer covered by <i>Sphagnum</i> and feather mosses	4.5	18
Paludified spruce forest	Peatland with a canopy cover of spruces at least 5%; other trees can also exist; field layer dominated by forbs, graminoids and shrubs; ground layer covered by <i>Sphagnum</i> and feather mosses	2.0	12
Paludified mixed forest	Peatland with a canopy cover of spruces and birches at least 5%; other trees can also exist; field layer dominated by forbs, graminoids and shrubs; ground layer covered by <i>Sphagnum</i> and feather mosses	2.1	12
Paludified birch forest	Peatland with canopy cover of spruces and birches at least 5%; other trees can also exist; field layer dominated by forbs, graminoids and shrubs; ground layer covered by <i>Sphagnum</i> and feather mosses	0.6	9
Dwarf shrub bog	Peatland with little trees (< 1% coverage); field layer covered by evergreen and deciduous shrubs as well as herbs (esp. <i>Rubus chamaemorus</i>); ground layer covered by <i>Sphagnum</i> and feather mosses	1.3	9
Tall sedge fen	Open peatland; field layer dominated by grasses, also deciduous shrubs (e.g. <i>Betula nana</i> , <i>Salix</i> spp.) and forbs; ground layer covered by <i>Sphagnum</i> and wet brown mosses	5.1	30
Flark	Open peatland, often covered by water; field layer dominated by graminoids and forbs; ground layer covered by open water, bare peat and wet brown mosses	1.6	9
Willow thicket	1–2 m tall willow (<i>Salix</i> spp.) thickets along small streams within peatlands; graminoids and forbs may exist in the field layer; ground layer covered by water, wet brown mosses and <i>Sphagnum</i>	0.1	3
Tundra and treeline vegetation		13.9	33
Dry shrub tundra heath	Open tundra located on the top of the fells; field layer dominated by evergreen shrubs (esp. <i>Empetrum nigrum</i>); ground layer covered by lichen, feather mosses and rock	4.3	14
Moist shrub tundra heath	Open tundra located on the top of the fells; field layer dominated by deciduous shrubs (esp. <i>Vaccinium myrtillus</i>), also evergreen shrubs, forbs and graminoids exist; ground layer covered by feather mosses	3.4	7
Treeline forest	Sparse forest located between open tundra and forest; tree species include mountain birch (<i>Betula pubescens</i> subsp. <i>czerepanovii</i>), spruce and pine; field layer includes deciduous shrubs, forbs and graminoids; ground layer dominated by feather mosses	6.2	12
Water	Lakes, ponds and streams	0.2	0
Non-vegetated	Non-vegetated areas, such as rock, sand and gravel roads	0.7	0

temperature and moisture next to the chamber at the surface (WET-2 sensor, Delta-T Devices Ltd, Cambridge, UK). Additionally, we recorded 5 cm soil temperature (Pt-100 RTD Thermometer HH376, Omega, Taiwan).

CH₄ flux (F) was calculated according to ideal gas law:

$$F = \left(\frac{dC(t)}{dt} \right)_{t=0} \frac{MPV}{RTA} \quad (1)$$

where $\left(\frac{dC(t)}{dt} \right)_{t=0}$ is the time derivative (ppm s⁻¹) of exponential regression (e.g. Korkiakoski et al. 2017) at the beginning of the closure, M is the molecular mass of CH₄ (16.042 g mol⁻¹), P is the air pressure (Pa) measured from the nearby official weather station (Kenttäröva, < 2 km from the flux measurements), R is the universal gas constant (8.314 J mol⁻¹ K⁻¹), T is the chamber headspace temperature (K), V and A are the chamber volume (m³) and base area (m²), respectively. Here, a micrometeorological sign convention is used where a positive flux indicates a flux from the ecosystem to the atmosphere (CH₄ emission/source) and a negative flux indicates a flux from the atmosphere to the ecosystem (CH₄ uptake/sink). To control for diurnal variation and changing weather conditions, we standardized the CH₄ fluxes to 10 °C soil temperature. We measured fluxes in 84 (30%) of the subplots 9–10 times between June and August and in the rest only once between July 3 and 13, 2019. For the subplots with repeated measurements, we estimated $F_{CH_4,10c}$ by using Arrhenius model:

$$F_{CH_4,meas} = F_{CH_4,10c} Q_{10}^{\frac{T-283.15}{10}} \quad (2)$$

where $F_{CH_4,meas}$ is the measured CH₄ flux, T is the soil temperature (K) at 5 cm, $F_{CH_4,10c}$ is the CH₄ flux at 10 °C and Q_{10} is the coefficient describing flux sensitivity to temperature. We kept Q_{10} and $F_{CH_4,10c}$ as free parameters during fitting. For the subplots with no repeated measurements, we solved $F_{CH_4,10c}$ directly from Eq. (2) by using median Q_{10} estimated from repeated measurements (2.149 for $F_{CH_4,meas} < 0$ and 2.386 for $F_{CH_4,meas} > 0$) and measured T and $F_{CH_4,meas}$.

Remote sensing data

We acquired diverse remote sensing datasets to map land cover, moisture and topography patterns within the study area (Table 2). For predicting CH₄ flux patterns, we were primarily interested in analyzing the applicability of optical Sentinel-2 satellite images and Sentinel-1 SAR data (European Space Agency, ESA) as well as a lidar-based digital terrain model (DTM, National Land Survey of Finland, NLS). In addition, we included canopy and intensity metrics from aerial lidar data, spectral and textural features from an aerial orthophoto (NLS), and spectral indices from PlanetScope satellite images (Planet Labs Inc., San Francisco, CA, USA) in the analysis. All optical remote sensing data (Sentinel-2, orthophoto, PlanetScope) were cloud-free. For each field inventory plot, we calculated features from each dataset.

Sentinel-2 satellites carry optical instruments detecting reflected solar radiation from the Earth's surface at 13 different wavelength bands (Drusch et al. 2012). Optical data can be used to differentiate vegetation and land cover types, due to diverging reflectance properties of landscape elements. We used the bottom-of-atmosphere reflectance Sentinel-2 image (Level-2A; atmospherically corrected with ESA's Sen2Cor algorithm) taken during our fieldwork (July 8). We included 11 bands (excluding bands 8a and 10, i.e. narrow near-infrared and cirrus respectively) in the analysis and also calculated 29 different widely used spectral indices (Table S1) with RStoolbox (Leutner et al. 2019) in R. These included indices that capture vegetation greenness and plant community composition such as normalized difference vegetation index (Rouse et al. 1974; Pettorelli et al. 2005; McPartland et al. 2019), and soil moisture such as water indices (Gao 1996; McFeeters 1996; Arroyo-Mora et al. 2018).

Sentinel-1 satellites carry C-band SAR instruments emitting microwave pulses at a central frequency of 5.405 GHz and measuring their backscatter characteristics (Torres et al. 2012). The backscatter is sensitive to land surface roughness, vegetation structure and in particular moisture and water (Widhalm et al. 2015; Bourgeau-Chavez et al. 2016; Millard and Richardson 2018; Karlson et al. 2019; Minasny et al. 2019). Backscatter is also dependent on incidence angle, and it thus has been recommended to use data with multiple incidence angles (O'Grady et al. 2014;

Table 2 Details of the remote sensing data

Dataset	Date	Producer	Spatial resolution	Number and list of layers and metrics
Aerial orthophoto	Jul 1 2018	National Land Survey of Finland	0.5 m	36: four spectral layers (R, G, B, NIR), eight GLCM texture layers for each band
Lidar digital terrain model	Jul 12 2018	National Land Survey of Finland	0.5 points m ⁻² (point cloud), 2 m (layers)	10: Elevation, slope, aspect, 5 TPIs (5 m, 10 m, 20 m, 50 m, 100 m neighbourhood radiuses), TWI, 2 DTWs (stream networks based on the digital terrain model (DTW-DTM) and topographic database (DTW-NLS))
Lidar intensity and canopy height model	Jul 12 2018	National Land Survey of Finland	0.5 points m ⁻² (point cloud), 2 m (layers)	3: Canopy height model, intensity for all returns, intensity for ground returns
Lidar canopy metrics	Jul 12 2018	National Land Survey of Finland	0.5 points m ⁻² (point cloud)	7 metrics for > 1.37 m tall trees: μ , SD, min, max, kurtosis, canopy cover %, density %
Six PlanetScope images	May 20 2019 Jun 16 2019 Jul 8 2019 Jul 26 2019 Aug 4 2019 Sep 5 2019	Planet Labs Inc	3 m	18: three spectral indices (GRVI, NDVI, NDWI) for all six images
Sentinel-2	Jul 8 2019	European Space Agency	10 m (B, G, R, NIR); 20 m (three red-edge bands and two SWIR bands); 60 m coastal aerosol, water vapor)	40: 11 bands and 29 spectral indices (CLG, CLRE, CTVI, DVI, EVI, GEMI, GNDVI, GRVI, MCARI, MNDWI, MSAVI, MSAVI2, MTCI, NBRI, NDREI1, NDREI2, NDVI, NDWI, NDWI2, NRVI, REIP, RVI, SATVI, SAVI, SLAVI, SR, TTVI, TVI, WDV1)
Sentinel-1	Jul 7–9 2019	European Space Agency	10 m	30: VH and VV polarization GRD images from three consecutive days, generalized using mean filter with five different window sizes (3 × 3, 5 × 5, 7 × 7, 9 × 9, 11 × 11)

Sentinel-2 indices are specified in Table S1

B blue, *DTW* depth to water, *G* green, *GLCM* grey-level co-occurrence matrix, *GRD* ground range detected, *GRVI* green–red vegetation index, *NDVI* normalized difference vegetation index, *NDWI* normalized difference water index, *NIR* near infra-red, *R* red, *SD* standard deviation, *TPI* topographical position index, *TWI* topographic wetness index, *VH* vertical transmit, horizontal receive, *VV* vertical transmit, vertical receive, μ mean

Millard and Richardson 2018). We acquired ground range Sentinel-1 data from three consecutive days (July 7–July 9), each taken in the morning but with different incidence angles (mean values 34.2°, 39.4°

and 44.1° respectively). We corrected the datasets geometrically with the help of the DTM and nearest neighborhood resampling and resampled the data to 10 m spatial resolution. We used both VH (vertical

transmit, horizontal receive) and VV (vertical transmit, vertical receive) polarized bands, and reduced speckle using mean filter with five different window sizes (3×3 , 5×5 , 7×7 , 9×9 , 11×11) (Table 2).

Topography is a major factor controlling soil moisture and hydrological patterns within landscapes (Murphy et al. 2007; Lidberg et al. 2020). From the topographic DTM, we calculated following layers with SAGA-GIS (Conrad et al. 2015): elevation, slope, topographic position indices with different neighborhood distances (Guisan et al. 1999), topographic wetness index (TWI, Böhner and Selige 2006) and two depth to water (DTW) indices with stream networks derived from DTM with minimum 4 ha catchment area (DTW-DTM) and NLS topographic database (DTW-NLS) respectively (Murphy et al. 2007). Of these predictors, in particular TWI and DTW have been shown to be useful in predicting spatial patterns of wetness (Murphy et al. 2007; Lidberg et al. 2020) and position index has been found to be function well in locating wetlands in depressions (Riley et al. 2017).

As forest structure differs between forests on mineral soil and peatlands (Thompson et al. 2016), we also calculated seven canopy metrics from the lidar point cloud for each larger plot using LAStools (Isenburg 2018) (Table 2). We also included two lidar intensity layers (all returns and ground returns only) whose functionality in wet area mapping has been documented (Stevens and Wolfe 2012).

For each orthophoto band, we calculated eight different grey-level co-occurrence matrix texture layers, since the quantification of pixel value neighborhood patterns (i.e. texture) has shown to increase distinctiveness between different land covers (Hall-Beyer 2017). The layers were energy, entropy, correlation, inverse difference moment, inertia, cluster shade, cluster prominence and Haralick correlation (Haralick et al. 1973) calculated with Orfeo ToolBox (Grizonnet et al. 2017).

Wet and dry areas have disparate seasonal cycles in their spectral properties, and it has been suggested that multi-temporal imagery should be used (Halabisky et al. 2018). Therefore, we used six PlanetScope images, each from a different phenological stage. The images were delivered as orthorectified surface reflectance products. To correct the minor geometrical errors and match the data with the orthophoto, we

geometrically corrected the images with 12 reference points by using a combination of polynomial transformation and a triangulated irregular network interpolation as well as nearest neighbor resampling. For each image, we calculated two vegetation indices capable of capturing vegetation phenological dynamics, i.e. normalized difference vegetation index (Rouse et al. 1974; McPartland et al. 2019), and green–red vegetation index (Gitelson et al. 2002; Anderson et al. 2016), and one water index, i.e. normalized difference water index (McFeeters 1996) (Table 2).

CH₄ regressions and upscaling with maps

We evaluated how much variance of measured CH₄ fluxes can be explained with different explanatory predictor sets and what kind of differences there are in the upscaled landscape-level fluxes and their spatial patterns when using 20 different CH₄ maps. We constructed the first map with the land cover classification so that we assigned the mean measured CH₄ flux estimate for each land cover type (classification accuracy 76%, Table 1, Fig. 1, Supplementary material). The following 19 maps were generated with regression-based techniques, in which predictors were remote sensing features and plot-based vegetation measures. We produced 15 maps in which we included all CH₄ measurement data ($n = 279$) in one regression (Table 3). Initially, we tested 14 different predictor set options, and we further tested if a smaller number of predictors would notably increase the regression performance ($> 3\%$ -point increase in explained variance) in each predictor set option. Consequently, we included a regression with three DTM-based predictors (elevation, TWI, DTW-NLS) as it had higher performance than regression with all DTM predictors. The subsequent four maps were produced so that we first divided the CH₄ measurement data before regressions into sinks ($n = 194$) and sources ($n = 85$). We tested two options for separating sinks and sources in the landscape: separation of sinks and sources based on land cover types (Table 1) and separation of sinks and sources with a binary classification in which training data consisted of CH₄ flux measurement plots. In the sink and source regressions, we tested two different predictor sets: all predictors and remote sensing predictors (i.e. options 1 and 3 in Table 3).

Table 3 Datasets included as explanatory predictors in different random forest models

	Regression no	Vegetation ^a	Sentinel-1	Sentinel-2	DTM	Other remote sensing ^b
	1	x	x	x	x	x
	2	x	—	—	—	—
	3	—	x	x	x	x
	4	—	x	—	—	—
	5	—	—	x	—	—
	6	—	—	—	x	—
	7	—	—	x	x	x
	8	—	x	—	x	x
	9	—	x	x	—	x
	10	—	x	x	—	—
	11	—	x	—	x	—
	12	—	—	x	x	—
	13	—	x	x	x	—
	14	—	—	—	—	x
	15	—	—	—	x ^c	—

^aIncludes plot-based vegetation measures of fuzzy plant community cluster membership values, PFT-specific and total biomass and leaf area index, and land cover classification

^bIncludes aerial orthophoto, lidar intensity and canopy metrics, and PlanetScope imagery

^cOnly three DTM features: elevation, TWI, DTW-NLS

To produce CH₄ maps other than land cover-based maps, we conducted random forest regressions (Breiman 2001) and binary classifications with 500 trees. Random forest is insensitive to overfitting and can thus be used in remote sensing analyses with several predictors (Belgiu and Dragut 2016). We tested one-third of all predictors at each tree node (square root of all predictors in binary classifications). We evaluated model performance with random forest out-of-bag assessment in which two-thirds of the data was used for training and the rest for validation for each tree. This method has been reported to result in a slightly conservative estimate of model performance (Clark et al. 2010). As the result of the random forest may slightly change between different random forest runs, we conducted 100 random forest runs for each predictor set option. For each regression, we calculated mean, minimum and maximum explained variance (random forest pseudo $R^2 = 1 - (\text{mean squared error})/(\text{variance}(\text{response}))$), root mean square error (RMSE) and normalized RMSE (nRMSE; i.e. RMSE divided by the range of observed values). For binary classifications, we calculated overall classification accuracy.

To remove irrelevant predictors from the final regressions and binary classifications, we reduced the number of predictors with Boruta (Kursa and Rudnicki 2010), which is a random forest wrapper predictor selection algorithm. We used mean decrease accuracy variable importance measure. We chose those

variables to final random forest models, which were not rejected during 999 random forest runs in Boruta (i.e. their importance was not statistically significantly lower than that of randomly shuffled shadow variables). We also calculated mean predictor importance scores over the Boruta runs, and Pearson correlation coefficients between the predictors and CH₄ flux. Analyses were conducted in R with packages randomForest (Liaw and Wiener 2002) and Boruta (Kursa and Rudnicki 2010).

For those remote-sensing based maps that included predictors only from one dataset and for maps combining Sentinel-1 and Sentinel-2 datasets, we produced pixel-based maps with the spatial resolution being as it was in the input data (Table 2). For the other regression-based maps, we utilized a geographic object-based image analysis approach with Baatz and Schäpe (2000) segmentation in TerraView (Câmara et al. 2008), and calculated similar predictors to each segment as for each field inventory plot (Table 2). For regressions including plot-based vegetation predictors, we utilized maps of those predictors (map production described in Supplementary material). We segmented the aerial orthophoto with the following parameter information: minimum segment size 100 (25 m²), similarity threshold 0.15, weight for color 0.75, and weight for compactness 0.5. The final average segment size was 50 m². Finally, to quantify differences in the spatial patterns between maps, we resampled all maps into 10 m resolution and

calculated a standard error of the mean map and pairwise Pearson correlation coefficients.

Results

The measured CH_4 fluxes at the catchment during the campaign in the first half of July 2019 varied between sinks and sources (-662 – $14,211 \mu\text{g CH}_4 \text{ m}^{-2} \text{ h}^{-1}$). In general, peatlands were sources (on average $2573 \mu\text{g CH}_4 \text{ m}^{-2} \text{ h}^{-1}$) while forests and tundra on mineral soil were sinks (on average -154 and $-133 \mu\text{g CH}_4 \text{ m}^{-2} \text{ h}^{-1}$ respectively) (Fig. 2, Table S11). However, some of the plots on drier peatlands (bogs and paludified forests) were weak sinks, and some of the plots on mineral soil were weak sources (Fig. 2).

Combined regressions for sinks and sources explained 59–76% of the variance in CH_4 fluxes, while sink regressions explained 21–24% and source regressions 58–59% (Table 4). In the binary sink and source classifications, mean classification accuracy was 96.5% (minimum to maximum 95.7–97.1%) and 96.6% (96.1–97.1%) in classification with all predictors and classification with remote sensing predictors, respectively.

In the regressions with all data, most of the regressions with remote sensing predictors only had higher performance than regressions with plot-based vegetation predictors. Nevertheless, the regression combining remote sensing and plot-based vegetation predictors had the highest performance (Table 4). Of the different remote sensing regressions, regression omitting DTM had the highest performance, and

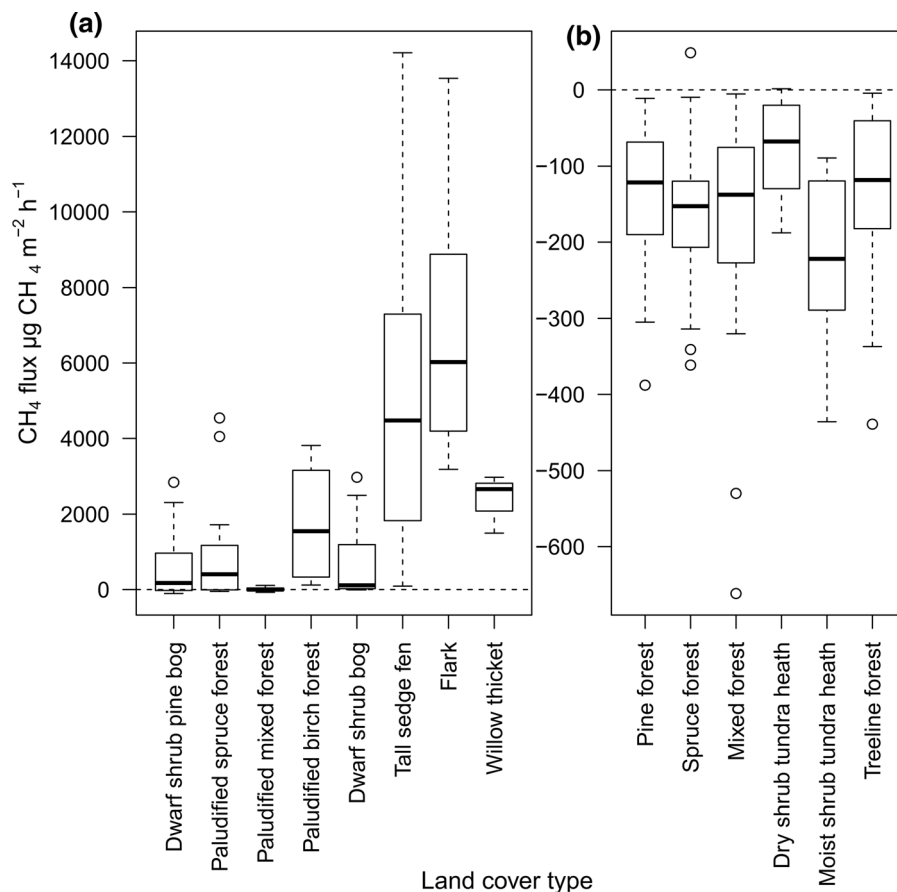


Fig. 2 Boxplot of measured CH_4 fluxes for each land cover type in **a** peatlands and **b** forest and tundra on mineral soil. Positive values indicate sources and negative values sinks. The number of observations is given in Table 1. The centerline presents

median, box interquartile range and whiskers extend 1.5 times the interquartile range. Observations beyond the whisker extent are plotted separately

Table 4 Mean percentage of explained variance, root mean squared error (RMSE) and normalized root mean squared error (nRMSE) over 100 random forest runs for each regression

Predictor set	Explained variance (%)	RMSE ($\mu\text{g m}^{-2} \text{h}^{-1}$)	nRMSE (%)	Predicted values for the catchment ($\mu\text{g m}^{-2} \text{h}^{-1}$)	CH ₄ sources (%)
All predictors	75.7 (74.5–76.9)	1179 (1149–1208)	7.9 (7.7–8.1)	379 (–277 to 8884)	29.8
Plot predictors	69.3 (68.1–70.3)	1325 (1302–1350)	8.9 (8.8–9.1)	277 (–284 to 9218)	27.0
Land cover map	n.a	n.a	n.a	304 (–224 to 6810)	17.4
Remote sensing based maps					
w/o DTM	74.4 (73.4–75.5)	1209 (1184–1232)	8.1 (8.0–8.3)	420 (–301 to 10,062)	38.5
All remote sensing data	74.1 (72.6–75.4)	1218 (1186–1251)	8.2 (8.0–8.4)	409 (–313 to 9310)	41.1
w/o Sentinel-2	74.1 (72.9–75.2)	1217 (1191–1243)	8.2 (8.0–8.4)	413 (–289 to 9274)	37.6
Sentinel-1 & DTM	73.2 (71.9–74.3)	1237 (1212–1267)	8.3 (8.1–8.5)	424 (–283 to 9072)	37.8
w/o Sentinel-1	72.9 (71.4–74.4)	1243 (1210–1279)	8.4 (8.1–8.6)	385 (–248 to 8973)	41.5
Sentinel-1 only	72.8 (71.8–73.8)	1247 (1224–1269)	8.4 (8.2–8.5)	502 (–311 to 9905)	46.7
Sentinel-1&2 & DTM	72.5 (71.2–73.7)	1254 (1226–1284)	8.4 (8.2–8.6)	402 (–313 to 9116)	41.8
Sentinel-1 & Sentinel-2	72.2 (71.2–73.4)	1260 (1234–1283)	8.5 (8.3–8.6)	444 (–287 to 10,178)	42.2
Sentinel-2 & DTM	71.0 (69.8–72.7)	1287 (1249–1313)	8.7 (8.4–8.8)	396 (–273 to 8836)	40.1
Elev & TWI & DTW	70.8 (69.7–71.9)	1292 (1268–1316)	8.7 (8.5–8.9)	426 (–381 to 10,861)	29.1
DTM only	67.3 (65.5–68.7)	1368 (1338–1404)	9.2 (9.0–9.4)	409 (–388 to 10,689)	32.4
Sentinel-2 only	66.7 (65.4–68.3)	1380 (1346–1406)	9.3 (9.0–9.5)	444 (–357 to 10,567)	49.6
w/o Sentinel-1&2 & DTM	59.3 (57.5–60.9)	1525 (1494–1559)	10.3 (10–10.5)	315 (–278 to 9380)	30.8
Sink and source regressions separately, with all predictors					
Sinks regressions	24.4 (23.0–26.0)	93 (92–93)	14.0 (13.8–14.1)		
Sources regressions	59.1 (57.4–61.5)	2164 (2099–2209)	15.2 (14.8–15.5)		
Sink and source from land cover map				303 (–292 to 9445)	17.4
Sink and source from binary map				253 (–292 to 9445)	12.1
Sink and source regressions separately, with remote sensing predictors					
Sinks regressions	20.8 (18.6–22.5)	95 (94–96)	14.3 (14.2–14.5)		
Sources regressions	57.5 (55.8–59.6)	2207 (2152–2250)	15.5 (15.1–15.8)		
Sink and source from land cover map				277 (–305 to 9252)	17.4

Table 4 continued

Predictor set	Explained variance (%)	RMSE ($\mu\text{g m}^{-2} \text{h}^{-1}$)	nRMSE (%)	Predicted values for the catchment ($\mu\text{g m}^{-2} \text{h}^{-1}$)	CH ₄ sources (%)
Sink and source from binary map				268 (−305 to 9252)	14.3

Minimum and maximum values are given in parentheses. In addition, predicted landscape-level mean CH₄ flux (landscape minimum and maximum in parentheses) and the proportion of area with net CH₄ emissions

regression omitting both Sentinel datasets and DTM had the worst performance. Relatively good performance was obtained in regressions with a single remote sensing data source, with Sentinel-1 having the highest performance followed by DTM and Sentinel-2. However, explanatory capacities were slightly higher when multiple data sources were included in a regression (Table 4).

The importance of Sentinel-1 and DTM in predicting CH₄ flux patterns was supported by predictor importance scores in which predictors calculated from these data were dominating among the top-ranked predictors in the regression including all remote sensing predictors (Fig. S1). For Sentinel-1, mean-filtered VH predictors from different incidence angles and window sizes were the most important ones. In the case of DTM, important predictors included those predicting wetness (TWI, DTW) as well as elevation and slope. For Sentinel-2, most important predictors included water vapor, blue and coastal aerosol bands and some spectral indices. In contrast, the role of other remote sensing-based predictors was small in the regression with all remote sensing predictors. In the correlation analysis, the presence of wetter fen plant community cluster, TWI, Sentinel-1 VH features, graminoid biomass and Sentinel-2 blue band had the highest absolute correlation with CH₄ (Table S12).

Although the proportion of area with net CH₄ emission was in minority within the landscape, the land area in total acted as a net source of CH₄ (Table 4). There was a considerable variation in the proportion of sources between different maps (12–50%), while the variation was in relative terms smaller in landscape-level mean flux estimations (253–502 $\mu\text{g CH}_4 \text{m}^{-2} \text{h}^{-1}$).

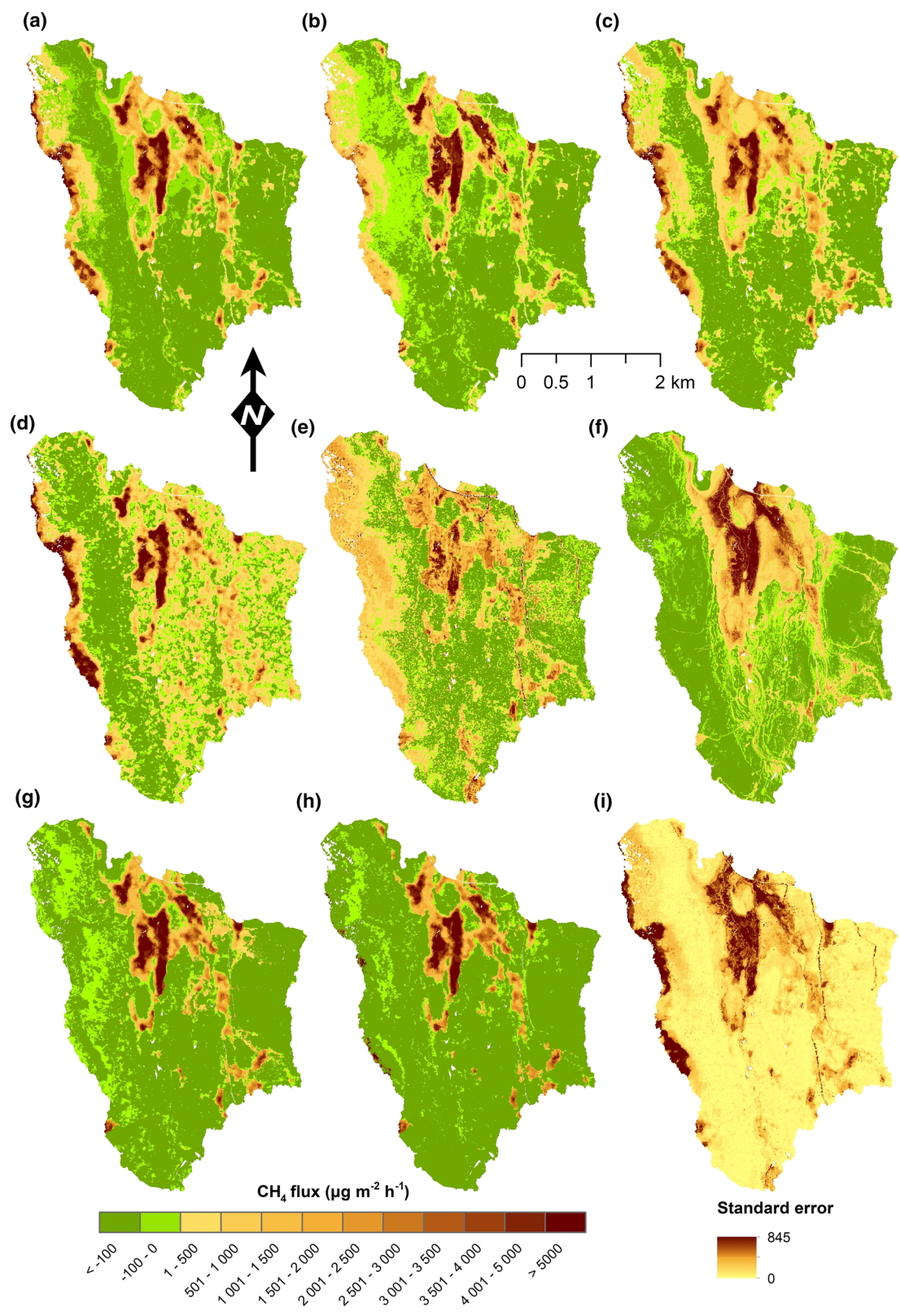
When visually interpreting the spatial patterns of CH₄, there were notable differences between maps produced with different predictor sets (Figs. 3, 4 and

Supplementary material). Most of the regression-based maps erroneously predicted CH₄ sources to mountain tundra in the western part of the study area. This pattern was the most evident with the Sentinel-1-based map (Fig. 3d), but not visible in the DTM-based maps (Fig. 3f), in land cover classification-based maps (Figs. 1, 2 and 3g) nor in binary classification-based maps (Fig. 3h). In the DTM-based maps, CH₄ sources were predicted to forests on mineral soil nearby peatlands in the middle part of the study area. Moreover, many other regression-based maps predicted CH₄ sources to forests on mineral soil that were CH₄ sinks according to our fieldwork data (Fig. 2).

According to the standard error map (Fig. 3i), differences between maps were the largest in the peatland areas, mountain tundra areas and roadsides. When looking at pairwise map comparisons, it could be seen that differences between maps were the largest between maps with predictors calculated from single remote sensing data source and similarities increased when maps with predictors calculated from multiple data sources were compared (Fig. 4).

In comparison to the land cover classification-based map, most of the regression-based maps overestimated landscape-level fluxes, and all regression-based maps considerably overestimated the proportion of sources. In contrast, separate sink and source regression-based maps slightly underestimated landscape-level fluxes

Fig. 3 Maps of predicted CH₄ fluxes based on **a** both remote sensing and vegetation predictors, **b** vegetation predictors, **c** all remote sensing predictors, **d** Sentinel-1, **e** Sentinel-2, and **f** digital terrain model, **g** sinks and sources derived from land cover classification and regressions with all predictors, **h** sinks and sources derived from binary classification and regressions with remote sensing predictors, **i** standard error map over all CH₄ maps. Positive values indicate sources and negative values sinks



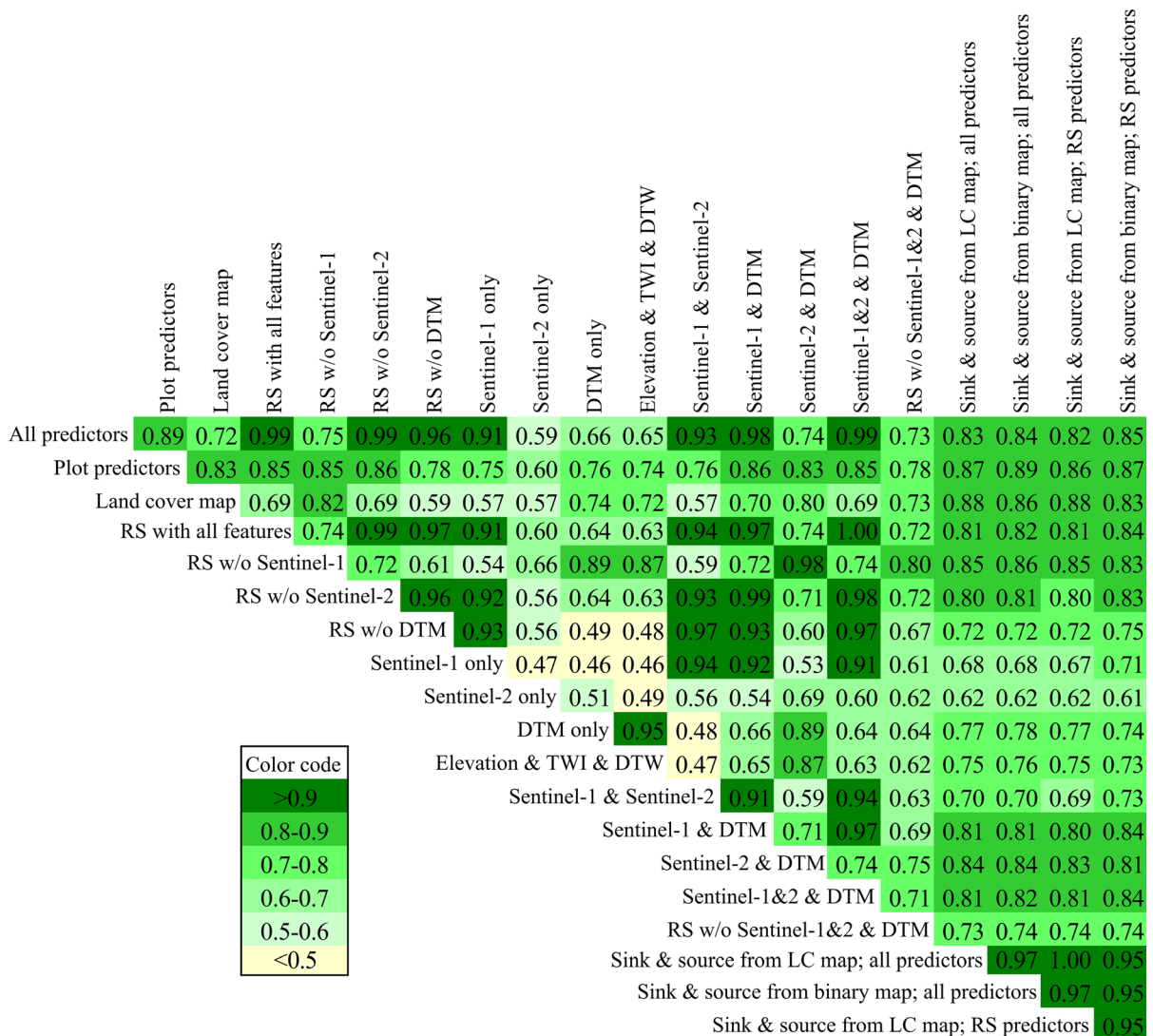


Fig. 4 Pairwise Pearson correlation coefficients between different maps. In the figure, LC refers to land cover and RS to remote sensing

and binary classifications proportion of sources (Table 4). Moreover, sink and source regression-based maps had the highest correlations with land cover-based map (Fig. 4).

Discussion and conclusions

According to our results, CH₄ fluxes can be predicted with a range of different remote sensing datasets, and remote sensing works better than plot-based vegetation measures in explaining CH₄ patterns (Table 4). The latter is a somewhat surprising result as vegetation

has been shown to be a major controlling factor of CH₄ fluxes (Turetsky et al. 2014; Abdalla et al. 2016). Furthermore, we assessed vegetation patterns in the plots where CH₄ fluxes were measured; thus, vegetation predictors were more directly linked to plot characteristics than remote sensing predictors. In upscaling, vegetation predictors and concurrent maps of vegetation have double uncertainty when compared to upscaling solely with remote sensing data as the vegetation maps need first to be produced with remote sensing data. Therefore, our results suggest that maps of vegetation may be an unnecessary step in an upscaling process. However, they are more useful

when the amount of sampled vegetation plots is larger than the number of chamber plots, which typically is the case when portable CH₄ measurement devices are not used.

In regressions with all data, explanatory capacities were relatively high (Table 4) which is probably linked to high spatial heterogeneity in terms of topography and land cover within the study area and also due to considerable range in CH₄ fluxes. In previous studies, relatively high explanatory capacities have been obtained when modeling CH₄ flux patterns with remote sensing data in study areas containing both peatlands and forests on mineral soil (Dinsmore et al. 2017). This explanation is further supported by the observation that the explanatory capacities were lower in the separate sink and source regressions in which within-regression landscape heterogeneity and range of fluxes were smaller than in the regressions with all data. Explanatory capacities were higher in source than in sink regressions which is logical as the range of fluxes were higher in source regressions and as peatlands—where the CH₄ sources are mainly located—are spatially heterogenic in terms of vegetation, topography and CH₄ fluxes. High classification accuracies in vegetation mapping have been previously obtained within peatlands (Lehmann et al. 2016; Räsänen and Virtanen 2019). To test how well upscaling can be performed within a single peatland, more studies employing spatially dense and extensive flux measurements should be conducted. Also, datasets should have ultra-high spatial resolution, preferably < 0.5 m grain size, due to fine-scale heterogeneities (Räsänen and Virtanen 2019).

The landscape-level mean fluxes were relatively similar in the different maps (i.e. similar landscape composition), and the landscape was a net source of CH₄ according to all maps. However, the spatial pattern differed strikingly between the maps (i.e. the difference in configuration) (Table 4, Figs. 3 and 4). The differences in spatial patterns were notably different in particular when looking at the threshold between sinks and sources. When compared to land cover and binary classification-based maps, regression-based maps overestimated the proportion of sources within the landscape and the mean CH₄ flux. On the one hand, the threshold between sinks and sources is probably most accurately predicted in the land cover or binary sink-source classification. This is because both land cover classification discriminating

peatlands (mostly sources) from mineral soils (mostly sinks) and binary classification had high classification accuracies. On the other hand, it is more difficult to judge which one of the landscape-level mean flux estimates is the most accurate. Although land cover classification-based map models well the threshold between sinks and sources, regression-based maps can assess the variation of CH₄ fluxes within specific land cover types. Therefore, the separate sink and source regression-based maps could provide the most accurate estimates of spatial patterns and landscape-level mean fluxes although the regression performance was lower in the separate sink and source regressions than in the regressions with all data. As the classification accuracy in the binary classification was high, we recommend using it in regression-based CH₄ map production instead of a land cover map as it requires smaller and simpler training data. Nevertheless, probably the most feasible option is to produce and compare multiple different maps to evaluate the composition and configuration of different processes and biogeochemical fluxes within various landscapes.

The most important remote sensing predictors included Sentinel-1 and topography. This is in line with earlier studies in which the locations of peatlands have been mapped with SAR and topographic data with relatively high accuracy (Murphy et al. 2007; Widhalm et al. 2015; Karlson et al. 2019; Lidberg et al. 2020). The highest accuracies were obtained when remote sensing predictors were included from multiple sources, but contrary to our expectations, boosts in explanatory capacities with multi-source data were relatively small (Table 4). Even with a single data source, in particular Sentinel-1, high accuracy was obtained, but accuracy dropped considerably when Sentinel-1, Sentinel-2 and topography were omitted from the models. Nonetheless, in pairwise map comparisons, the spatial patterns were considerably different between maps with predictors from a single data source. Similarities increased when maps with more predictors were compared (Fig. 4), which suggests that the prediction of spatial patterns is more robust with multi-source remote sensing. Therefore, in line with previous literature (Bourgeau-Chavez et al. 2016; Karlson et al. 2019; Räsänen and Virtanen 2019), it is advisable to use multiple data sources to get both high explanatory capacities and realistic predictions of spatial patterns of CH₄ fluxes.

When looking at the importance of different topography predictors, the regression model with only three topographic predictors (TWI, elevation, DTW-NLS) had a higher explanatory capacity than a model with more topographic predictors emphasizing the importance of these three predictors in CH₄ upscaling (Table 4). Of these predictors, TWI and DTW should in principle model soil wetness (Murphy et al. 2007; Lidberg et al. 2020) which is a key control of CH₄ fluxes (Turetsky et al. 2014; Abdalla et al. 2016).

When looking at Sentinel-1 predictors, VH predictors were more important than VV predictors which is in line with previous research (Baghdadi et al. 2001; Karlson et al. 2019). Our results also showed that multiple different VH predictors (i.e. VH mean-filtered with different window sizes and acquired with different incidence angles) were among the most important predictors. This suggests that it is preferable to test, and, if necessary, include multiple diverse SAR datasets and preprocessing options in peatland mapping. Additionally, as SAR is sensitive to temporal moisture conditions (Bourgeau-Chavez et al. 2013), data taken on different time-points, even consecutive days, can give divergent results. Further boosts in regression performance could have been obtained if we had included SAR datasets from early and late growing season and also from winter (Widhalm et al. 2015; Karlson et al. 2019). This could have alleviated problems related to mountain tundra, which was erroneously modeled to be a significant emitter of CH₄ in the Sentinel-1-based map. Nevertheless, it has been found that SAR backscatter is more sensitive to vegetation structure than soil moisture in peatland environments (Millard and Richardson 2018). Moreover, in a study that incorporated multi-temporal SAR data in peatland detection, open peatlands were mixed up with mountain tundra, and the misclassifications were reduced with the help of topographic predictors (Karlson et al. 2019).

Interestingly, of the Sentinel-2 predictors, the most important ones were water vapor, blue and coastal aerosol bands instead of predictors, which are usually important in vegetation mapping, such as greenness indices (Pettorelli et al. 2005), or water indices sensitive to soil moisture (Arroyo-Mora et al. 2018). Our results suggest that in CH₄ flux studies, four spectral bands is not sufficient, and higher spectral resolution should be included. This finding is further backed by the low importance of PlanetScope data

with four spectral bands in the regressions. When assessing CH₄ flux patterns within peatlands with fine-scale spatial heterogeneity, preferred datasets could be hyperspectral or multispectral sensors with at least ten spectral bands aboard unmanned aerial vehicles. However, the importance of different spectral features should be further researched; in particular because the most important spectral bands according to our study are primarily designated for atmospheric corrections (in particular water vapor and coastal aerosol bands) or are sensitive to atmospheric scattering even after the ESA Sen2Cor atmospheric correction (Drusch et al. 2012; Li et al. 2018).

There were some limitations in our study which should be addressed in future studies. Firstly, our measurement campaign covered only a snapshot situation during peak summer, and we did not quantify the seasonal or diurnal trends nor long-term balances of CH₄. The broad spatial flux patterns in fluxes would probably be more or less similar also when evaluating a longer time span, i.e. mineral soils and peatlands would act as sinks and sources, respectively, but there would be changes in the magnitude of the fluxes within the catchment as well as within the vegetation and land cover types. This is backed by previous studies, which have reported that seasonal variation in CH₄ flux is largely controlled by variation in soil and air temperature and moisture (Chi et al. 2020), whereas diurnal variation is correlated in addition with changes solar radiation and latent heat flux (Gažovic et al. 2010; Helbig et al. 2017; Long et al. 2010). These variables mainly affect the temporal trends in CH₄ fluxes, and spatial variation can mostly be explained by vegetation and land cover types (Forbrich et al. 2011; Davidson et al. 2016; Tuovinen et al. 2019; Chi et al. 2020); however, also soil temperatures may vary considerably between land cover types, in particular during summer (Helbig et al. 2017). Secondly, we omitted the fluxes originating from trees in our analysis. It has been shown that trees on mineral soil emit CH₄; for instance, emissions of an average Scots pine tree has been measured to be 0.8% of uptake by forest floor (Machacova et al. 2016). Therefore, future studies should concentrate on developing remote sensing-based spatiotemporal models for CH₄ and carbon balances that account for fluxes originating from open peatlands, forest floors and trees.

Recently developed portable carbon analyzers and modeling approaches presented in this article enable to

measure and model landscape-level variation of CH₄ dynamics in such detail that spatially explicit maps can be produced. The maps produced with high resolution remote sensing constrain uncertainties related to CH₄ fluxes and their spatial patterns. The approach presented is applicable at various spatial extents, but field observation data should be collected so that it is representative for the whole region of interest, and at smaller extents, finer resolution remote sensing data acquired for example from unmanned aerial vehicles should be used.

Acknowledgements We thank Viivi Lindholm, Annika Alsila, Petri Salovaara and Stephanie Gerin for assisting in the fieldwork, and Academy of Finland for funding (Grants 308513 [TV, AR] and 308511 [AL, TM, MK]).

Open Access This article is licensed under a Creative Commons Attribution 4.0 International License, which permits use, sharing, adaptation, distribution and reproduction in any medium or format, as long as you give appropriate credit to the original author(s) and the source, provide a link to the Creative Commons licence, and indicate if changes were made. The images or other third party material in this article are included in the article's Creative Commons licence, unless indicated otherwise in a credit line to the material. If material is not included in the article's Creative Commons licence and your intended use is not permitted by statutory regulation or exceeds the permitted use, you will need to obtain permission directly from the copyright holder. To view a copy of this licence, visit <http://creativecommons.org/licenses/by/4.0/>.

Funding Open Access funding provided by University of Helsinki including Helsinki University Central Hospital.

Data availability The datasets generated during and/or analyzed during the current study are available from the corresponding author on reasonable request.

References

- Abdalla M, Hastings A, Truu J, Espenberg M, Mander Ü, Smith P (2016) Emissions of methane from northern peatlands: a review of management impacts and implications for future management options. *Ecol Evol* 6:7080–7102
- Anderson HB, Nilsen L, Tommervik H, Karlsen SR, Nagai S, Cooper EJ (2016) Using ordinary digital cameras in place of near-infrared sensors to derive vegetation indices for phenology studies of high arctic vegetation. *Remote Sens* 8:847
- Arroyo-Mora JP, Kalacska M, Soffer RJ, Moore TR, Roulet NT, Juutinen S, Ifimov G, Leblanc G, Inamdar D (2018) Airborne hyperspectral evaluation of maximum gross photosynthesis, gravimetric water content, and CO₂ uptake efficiency of the Mer Bleue ombrotrophic peatland. *Remote Sens* 10:565
- Baatz M, Schäpe A (2000) Multiresolution segmentation—an optimization approach for high quality multi-scale image segmentation. In: Strobl J, Blaschke T, Griesebner G (eds) *Angewandte Geographische Informations-Verarbeitung XII*. Wichmann Verlag, Karlsruhe, pp 12–23
- Baghdadi N, Bernier M, Gauthier R, Neeson I (2001) Evaluation of C-band SAR data for wetlands mapping. *Int J Remote Sens* 22:71–88
- Belgiu M, Dragut L (2016) Random forest in remote sensing: a review of applications and future directions. *Isprs J Photogramm Remote Sens* 114:24–31
- Böhner J, Selige T (2006) Spatial prediction of soil attributes using terrain analysis and climate regionalisation. In: Böhner J, McCloy KR, Strobl J (eds) *SAGA—Analysis and modelling applications*, vol 115. Göttinger Geographische Abhandlungen, Göttingen, pp 13–28
- Bourgeau-Chavez LL, Leblon B, Charbonneau F, Buckley JR (2013) Assessment of polarimetric SAR data for discrimination between wet versus dry soil moisture conditions. *Int J Remote Sens* 34:5709–5730
- Bourgeau-Chavez LL, Endres S, Powell R, Battaglia MJ, Benscoter B, Turetsky M, Kasischke ES, Banda E (2016) Mapping boreal peatland ecosystem types from multitemporal radar and optical satellite imagery. *Can J For Res* 47:545–559
- Breiman L (2001) Random forests. *Mach Learn* 45:5–32
- Bruhwyler L, Dlugokencky E, Masarie K, Ishizawa M, Andrews A, Miller J, Sweeney C, Tans P, Worthy D (2014) CarbonTracker-CH₄: an assimilation system for estimating emissions of atmospheric methane. *Atmos Chem Phys* 14:8269–8293
- Câmara G, Vinhas L, Ferreira KR, Queiroz GRD, Souza RCMD, Monteiro AMV, Carvalho MTD, Casanova MA, Freitas UMD (2008) TerraLib: an open source GIS library for large-scale environmental and socio-economic applications. In: Hall GB, Leahy MG (eds) *Open source approaches in spatial data handling*. Springer, Berlin, pp 247–270
- Chi J, Nilsson MB, Laudon H, Lindroth A, Wallerman J, Fransson JES, Kljun N, Lundmark T, Ottosson Löfvenius M, Peichl M (2020) The Net Landscape Carbon Balance—Integrating terrestrial and aquatic carbon fluxes in a managed boreal forest landscape in Sweden. *Glob Change Biol* 26:2353–2367
- Clark ML, Aide TM, Grau HR, Riner G (2010) A scalable approach to mapping annual land cover at 250 m using MODIS time series data: a case study in the Dry Chaco ecoregion of South America. *Remote Sens Environ* 114:2816–2832
- Conrad O, Bechtel B, Bock M, Dietrich H, Fischer E, Gerlitz L, Wehberg J, Wichmann V, Böhner J (2015) System for automated geoscientific analyses (SAGA) v. 2.1.4. *Geosci Model Dev* 8:1991–2007
- Davidson SJ, Sloan VL, Phoenix GK, Wagner R, Fisher JP, Oechel WC, Zona D (2016) Vegetation type dominates the spatial variability in CH₄ emissions across multiple Arctic Tundra. *Landsc Ecosyst* 19:1116–1132
- Davidson SJ, Santos MJ, Sloan VL, Reuss-Schmidt K, Phoenix GK, Oechel WC, Zona D (2017) Upscaling CH₄ fluxes

- using high-resolution imagery in Arctic Tundra ecosystems. *Remote Sens* 9:227
- Dinsmore KJ, Drewer J, Levy PE, George C, Lohila A, Aurela M, Skiba UM (2017) Growing season CH₄ and N₂O fluxes from a subarctic landscape in northern Finland; From chamber to landscape scale. *Biogeosciences* 14:799–815
- Drusch M, Del Bello U, Carlier S, Colin O, Fernandez V, Gascon F, Hoersch B, Isola C, Laberinti P, Martimort P, Meygret A, Spoto F, Sy O, Marchese F, Bargellini P (2012) Sentinel-2: ESA's optical high-resolution mission for GMES operational services. *Remote Sens Environ* 120:25–36
- Forbrich I, Kutzbach L, Wille C, Becker T, Wu J, Wilmking M (2011) Cross-evaluation of measurements of peatland methane emissions on microform and ecosystem scales using high-resolution landcover classification and source weight modelling. *Agric For Meteorol* 151:864–874
- Frolking S, Talbot J, Jones MC, Treat CC, Kauffman JB, Tuittila E-S, Roulet N (2011) Peatlands in the Earth's 21st century climate system. *Environ Rev* 19:371–396
- Gao BC (1996) NDWI—a normalized difference water index for remote sensing of vegetation liquid water from space. *Remote Sens Environ* 58:257–266
- Gažovic M, Kutzbach L, Schreiber P, Wille C, Wilmking M (2010) Diurnal dynamics of CH₄ from a boreal peatland during snowmelt. *Tellus B* 62:133–139
- Gitelson AA, Kaufman YJ, Stark R, Rundquist D (2002) Novel algorithms for remote estimation of vegetation fraction. *Remote Sens Environ* 80:76–87
- Grizonnet M, Michel J, Poughon V, Inglada J, Savinaud M, Cresson R (2017) Orfeo ToolBox: open source processing of remote sensing images Open Geospatial Data. *Softw Standards* 2:15
- Guisan A, Weiss SB, Weiss AD (1999) GLM versus CCA spatial modeling of plant species distribution. *Plant Ecol* 143:107–122
- Halabisky M, Babcock C, Moskal LM (2018) Harnessing the temporal dimension to improve object-based image analysis classification of wetlands. *Remote Sens* 10:1467
- Hall-Beyer M (2017) Practical guidelines for choosing GLCM textures to use in landscape classification tasks over a range of moderate spatial scales. *Int J Remote Sens* 38:1312–1338
- Haralick RM, Dinstein I, Shanmugam K (1973) Textural features for image classification. *IEEE Trans Syst Man Cybern* 6:610–621
- Helbig M, Chasmer LE, Kljun N, Quinton WL, Treat CC, Sonnentag O (2017) The positive net radiative greenhouse gas forcing of increasing methane emissions from a thawing boreal forest-wetland landscape. *Glob Change Biol* 23:2413–2427
- IPCC (2013) Summary for policymakers. In: Stocker T, Qin D, Plattner G, Tignor M, Allen S, Boschung J, Nauels A, Xia Y, Bex B, Midgley B (eds) *Climate change 2013: the physical science basis. Contribution of working group I to the fifth assessment report of the intergovernmental panel on climate change*. Cambridge University Press, Cambridge, UK and New York, NY, USA
- Isenburg M (2018) LAStools—efficient LiDAR processing software (version 180429, unlicensed). <http://rapidlasso.com/LAStools>.
- Karlson M, Gålfalk M, Crill P, Bousquet P, Saunois M, Bastviken D (2019) Delineating northern peatlands using Sentinel-1 time series and terrain indices from local and regional digital elevation models. *Remote Sens Environ* 231:111252
- Kedron PJ, Frazier AE, Ovando-Montejo GA, Wang J (2018) Surface metrics for landscape ecology: a comparison of landscape models across ecoregions and scales. *Landsc Ecol* 33:1489–1504
- Korkiakoski M, Tuovinen JP, Aurela M, Koskinen M, Minkinen K, Ojanen P, Penttilä T, Rainne J, Laurila T, Lohila A (2017) Methane exchange at the peatland forest floor—automatic chamber system exposes the dynamics of small fluxes. *Biogeosciences* 14:1947–1967
- Kursa MB, Rudnicki WR (2010) Feature selection with the Boruta Package. *J Stat Softw* 36:1–13
- Lai DYF (2009) Methane dynamics in Northern Peatlands: a review. *Pedosphere* 19:409–421
- Le Mer J, Roger P (2001) Production, oxidation, emission and consumption of methane by soils: a review. *Eur J Soil Biol* 37:25–50
- Lehmann JRK, Münchberger W, Knoth C, Blodau C, Nieberding F, Prinz T, Pancotto VA, Kleinebecker T (2016) High-resolution classification of south patagonian peat bog microforms reveals potential gaps in up-scaled CH₄ fluxes by use of Unmanned Aerial System (UAS) and CIR imagery. *Remote Sens* 8:173
- Leutner B, Horning N, Schwalb-Willman J (2019) RStoolbox: tools for remote sensing data analysis R package version 026
- Li Y, Chen J, Ma Q, Zhang HK, Liu J (2018) Evaluation of sentinel-2A surface reflectance derived using Sen2Cor in North America. *IEEE J Sel Topics Appl Earth Observ Remote Sens* 11:1997–2021
- Liaw A, Wiener M (2002) Classification and regression by random. *For R News* 2:18–22
- Lidberg W, Nilsson M, Ågren A (2020) Using machine learning to generate high-resolution wet area maps for planning forest management: a study in a boreal forest landscape. *Ambio* 49:475–486
- Lohila A, Penttilä T, Jortikka S, Aalto T, Anttila P, Asmi E, Aurela M, Hatakka J, Hellen H, Henttonen H, Hanninen P, Kilkki J, Kyllonen K, Laurila T, Lepistö A, Lihavainen H, Makkonen U, Paatero J, Rask M, Sutinen R, Tuovinen JP, Vuorenmaa J, Viisanen Y (2015) Preface to the special issue on integrated research of atmosphere, ecosystems and environment at Pallas Boreal. *Environ Res* 20:431–454
- Lohila A, Aalto T, Aurela M, Hatakka J, Tuovinen J-P, Kilkki J, Penttilä T, Vuorenmaa J, Hänninen P, Sutinen R, Viisanen Y, Laurila T (2016) Large contribution of boreal upland forest soils to a catchment-scale CH₄ balance in a wet year. *Geophys Res Lett* 43:2946–2953
- Long KD, Flanagan LB, Cai T (2010) Diurnal and seasonal variation in methane emissions in a northern. *Can Peatl Meas Eddy Covar* 16:2420–2435
- Machacova K, Bäck J, Vanhatalo A, Halmeenmäki E, Kolari P, Mammarella I, Pumpanen J, Acosta M, Urban O, Pihlatie M (2016) *Pinus sylvestris* as a missing source of nitrous oxide and methane in boreal forest. *Sci Rep* 6:23410

- McFeeters SK (1996) The use of the Normalized Difference Water Index (NDWI) in the delineation of open water features. *Int J Remote Sens* 17:1425–1432
- McGarigal K, Tagil S, Cushman SA (2009) Surface metrics: an alternative to patch metrics for the quantification of landscape structure. *Landsc Ecol* 24:433–450
- McPartland MY, Kane ES, Falkowski MJ, Kolka R, Turetsky MR, Palik B, Montgomery RA (2019) The response of boreal peatland community composition and NDVI to hydrologic change, warming, and elevated carbon dioxide. *Glob Change Biol* 25:93–107
- Millard K, Richardson M (2018) Quantifying the relative contributions of vegetation and soil moisture conditions to polarimetric C-Band SAR response in a temperate peatland. *Remote Sens Environ* 206:123–138
- Minasny B, Berglund Ö, Connolly J, Hedley C, de Vries F, Gimona A, Kempen B, Kidd D, Lilja H, Malone B, McBratney A, Roudier P, O'Rourke S, Rudiyanto PJ, Poggio L, ten Caten A, Thompson D, Tuve C, Widyatmanti W (2019) Digital mapping of peatlands—a critical review earth. *Sci Rev* 196:102870
- Morozumi T, Shingubara R, Suzuki R, Kobayashi H, Tei S, Takano S, Fan R, Liang M, Maximov TC, Sugimoto A (2019) Estimating methane emissions using vegetation mapping in the taiga–tundra boundary of a north-eastern Siberian lowland. *Tellus B* 71:1581004
- Murphy PNC, Ogilvie J, Connor K, Arp PA (2007) Mapping wetlands: a comparison of two different approaches for New Brunswick, Canada. *Wetlands* 27:846–854
- O'Grady D, Leblanc M, Bass A (2014) The use of radar satellite data from multiple incidence angles improves surface water mapping. *Remote Sens Environ* 140:652–664
- Pettorelli N, Vik JO, Mysterud A, Gaillard J-M, Tucker CJ, Stenseth NC (2005) Using the satellite-derived NDVI to assess ecological responses to environmental change. *Trends Ecol Evol* 20:503–510
- Räsänen A, Virtanen T (2019) Data and resolution requirements in mapping vegetation in spatially heterogeneous landscapes. *Remote Sens Environ* 230:111207
- Riley JW, Calhoun DL, Barichivich WJ, Walls SC (2017) Identifying small depressional wetlands and using a topographic position index to infer hydroperiod regimes for pond-breeding amphibians. *Wetlands* 37:325–338
- Rouse JWJ, Haas RH, Schell JA, Deering DW (1974) Monitoring vegetation systems in the Great Plains with ERTS. Paper presented at the Third Earth Resources Technology Satellite-1 Symposium, Washington, DC, 10–14 December 1973
- Stevens CW, Wolfe SA (2012) High-resolution mapping of wet terrain within discontinuous permafrost using LiDAR intensity. *Permafrost Periglac Process* 23:334–341
- Thompson DK, Simpson BN, Beaudoin A (2016) Using forest structure to predict the distribution of treed boreal peatlands in Canada. *For Ecol Manag* 372:19–27
- Thorpe AK, Frankenberg C, Aubrey AD, Roberts DA, Nottrott AA, Rahn TA, Sauer JA, Dubey MK, Costigan KR, Arata C, Steffke AM, Hills S, Haselwimmer C, Charlesworth D, Funk CC, Green RO, Lundeen SR, Boardman JW, Eastwood ML, Sarture CM, Nolte SH, McCubbin IB, Thompson DR, McFadden JP (2016) Mapping methane concentrations from a controlled release experiment using the next generation airborne visible/infrared imaging spectrometer (AVIRIS-NG). *Remote Sens Environ* 179:104–115
- Torres R, Snoeij P, Geudtner D, Bibby D, Davidson M, Attema E, Potin P, Rommen B, Floury N, Brown M, Traver IN, Deghaye P, Duesmann B, Rosich B, Miranda N, Bruno C, L'Abbate M, Croci R, Pietropaolo A, Huchler M, Rostan F (2012) GMES Sentinel-1 mission. *Remote Sens Environ* 120:9–24
- Tuovinen JP, Aurela M, Hatakka J, Räsänen A, Virtanen T, Mikola J, Ivakhov V, Kondratyev V, Laurila T (2019) Interpreting eddy covariance data from heterogeneous Siberian tundra: land-cover-specific methane fluxes and spatial representativeness. *Biogeosciences* 16:255–274
- Turetsky MR, Kotowska A, Bubier J, Dise NB, Crill P, Hornibrook ERC, Minkinen K, Moore TR, Myers-Smith IH, Nykänen H, Olefeldt D, Rinne J, Saarnio S, Shurpali N, Tuittila E-S, Waddington JM, White JR, Wickland KP, Wilmsking M (2014) A synthesis of methane emissions from 71 northern, temperate, and subtropical wetlands. *Glob Change Biol* 20:2183–2197
- Widhalm B, Bartsch A, Heim B (2015) A novel approach for the characterization of tundra wetland regions with C-band SAR satellite data. *Int J Remote Sens* 36:5537–5556

Publisher's Note Springer Nature remains neutral with regard to jurisdictional claims in published maps and institutional affiliations.